

I. Graur, T. Veltzke, J. G. Méolans, M. T. Ho, J. Thöming

The gas flow diode effect: theoretical and experimental analysis of moderately rarefied gas flows through a microchannel with varying cross section

Journal Article as: peer-reviewed accepted version (Postprint)

DOI of this document\* (secondary publication): <https://doi.org/10.26092/elib/2442>

Publication date of this document: 07/09/2023

\* for better findability or for reliable citation

#### Recommended Citation (primary publication/Version of Record) incl. DOI:

Graur, I., Veltzke, T., Méolans, J.G. et al. The gas flow diode effect: theoretical and experimental analysis of moderately rarefied gas flows through a microchannel with varying cross section. *Microfluid Nanofluid* 18, 391-402 (2015). <https://doi.org/10.1007/s10404-014-1445-4>

Please note that the version of this document may differ from the final published version (Version of Record/primary publication) in terms of copy-editing, pagination, publication date and DOI. Please cite the version that you actually used. Before citing, you are also advised to check the publisher's website for any subsequent corrections or retractions (see also <https://retractionwatch.com/>).

"This version of the article has been accepted for publication, after peer review (when applicable) and is subject to Springer Nature's AM terms of use, which permit users to view, print, copy, download and text and data-mine the content, for the purposes of academic research, subject always to the full conditions of use. Under no circumstances may the AM be shared or distributed under a Creative Commons, or other form of open access license, nor may it be reformatted or enhanced. It's not the Version of Record and does not reflect post-acceptance improvements, or any corrections. The Version of Record is available online at: <https://doi.org/10.1007/s10404-014-1445-4>."

This document is made available with all rights reserved.

#### Take down policy

If you believe that this document or any material on this site infringes copyright, please contact [publizieren@suub.uni-bremen.de](mailto:publizieren@suub.uni-bremen.de) with full details and we will remove access to the material.

# The gas flow diode effect: theoretical and experimental analysis of moderately rarefied gas flows through a microchannel with varying cross section

I. Graur · T. Veltzke · J. G. Méolans ·  
M. T. Ho · J. Thöming

Received: 3 February 2014 / Accepted: 10 June 2014 / Published online: 20 June 2014

**Abstract** Moderately rarefied gas flows are clearly distinguished from viscous flow in the continuum regime and from free molecular flow at high rarefaction. Being of relevance for various technical applications, the understanding of such flow processes is crucial for considerable enhancement in micro electromechanical systems (MEMS) and vacuum techniques. In this work, we focus on the isothermal rarefied gas flow through long channels with longitudinally varying cross section. We apply two approaches, an analytical one and a numerical one that is based on the solution of the linearized S-model, both allowing us to predict the mass flow rate in diverging and converging flow directions for arbitrary pressure gradients. Both approaches are validated by CO<sub>2</sub>, N<sub>2</sub> and Ar permeation experiments on tapered microchannels manufactured by means of micromilling. The local Knudsen numbers ranged from 0.0471 to 0.2263. All the numerical and analytical results are in good agreement to the experimental data and show that the mass flow rate is significantly higher

when the duct is perfused in converging direction. The understanding of the physical phenomenon of this gas flow diode effect might pave the way for novel components in MEMS such as static one-way valves.

**Keywords** Rarefied gas · Long tapered channel · Gas flow diode effect · Microchannel production · Mass flow rate measurement

## 1 Introduction

The flow of rarefied gases through a long channel with rectangular cross section is a practical problem in the field of micro electromechanical systems (MEMS) and in vacuum technology applications. This kind of flow was widely studied on the basis of the kinetic theory, and a detailed review is given in Sharipov and Seleznev (1998). Also a vast amount of experiments on microducts with various but *uniform* cross section were performed in the last decades (Porodnov et al. 1974; Aubert and Colin 2001; Colin et al. 2004; Ewart et al. 2007; Graur et al. 2009; Veltzke 2013).

In several applications, however, the cross section varies alongside the channel. As examples of such kind of flow, the leakage through compressor valves (de Silva and Deschamps 2012) and the flow in the microbearing (Stevanovic 2007; Stevanovic and Djordjevic 2012) may be given. Only few numerical simulations are carried out on the flow through ducts with variable conical and tapered rectangular cross sections (Aubert et al. 1998; Sharipov and Bertoldo 2005; Titarev et al. 2013; Graur and Ho 2014). It was found that the permeability is higher when the duct is perfused in converging direction (Aubert et al. 1998; Veltzke et al. 2012; Veltzke 2013). In a more general

---

I. Graur · J. G. Méolans · M. T. Ho  
CNRS, IUSTI UMR 7343, Aix-Marseille Université,  
13453 Marseille, France  
e-mail: irina.martin@univ-amu.fr

J. G. Méolans  
e-mail: joseph.meolans@univ-amu.fr

M. T. Ho  
e-mail: mtho@polytech.univ-mrs.fr

T. Veltzke (✉) · J. Thöming  
Center for Environmental Research and Sustainable  
Technology (UFT), University of Bremen,  
Leobener Strasse 1, 28359 Bremen, Germany  
e-mail: tveltzke@uni-bremen.de

J. Thöming  
e-mail: thoeming@uni-bremen.de

sense, the non-symmetric behavior of the flow following the direction (diode effect) was firstly investigated in the liquid flows, notably by the authors of Stemme and Stemme (1993), Lee and Azid (2009). More recently, in case of gaseous flows, this *gas flow diode effect* was found to increase with rarefaction in the slip flow regime and to disappear in the continuum regime (Veltzke 2013). When the both ends of a channel are in the free molecular regime, this effect theoretically should not exist, too (Sharipov and Bertoldo 2005; Graur and Ho 2014).

Based on these considerations and previous experimental observations (Veltzke 2013; Veltzke et al. 2012), we present an analytical model for the isothermal pressure-driven flow in ducts with alongside varying cross section. In this work, we apply the approach based on the solution of the Stokes equation subjected to the velocity slip boundary condition. We solve this model for the predictive calculation of the flow through a long channel with variable rectangular cross section.

In addition, and for further validation, the numerical approach developed in Graur and Ho (2014) is used. This approach allows to calculate the mass flow rate through a long channel with variable rectangular cross section for arbitrary pressure and temperature drops over a wide range of gaseous rarefaction.

Both analytical and numerical solutions are compared with one another and with experimental data for the CO<sub>2</sub>, N<sub>2</sub> and Ar gas flow through a micromilled channel of varying rectangular cross section.

## 2 Model development

### 2.1 Problem statement

A long channel of variable cross section connects two reservoirs containing the same gas. The channel width  $w$  is supposed to remain constant alongside the channel, while the channel height  $h$  varies from  $h_1$  in the first reservoir to  $h_2$  ( $h_2 \geq h_1$ ) in the second reservoir, with  $\max(h) \leq w$  (Fig. 1). One reservoir is maintained at the pressure  $p_1$ , while the pressure in the other reservoir is  $p_2$ , respectively. We further assume isothermal conditions in the complete system and the channel to be long enough ( $\max(h) \ll L$ ) so that the end effects can be neglected.

### 2.2 Analytical solution for the slip flow regime

In this section, we derive the analytical model for the previously stated flow configuration. Here we assume that  $\max(h) \ll w$  to treat the flow as two-dimensional.

In the hydrodynamic flow regime ( $Kn \rightarrow 0$ ) the flow velocity  $u$  in the  $x$ -direction through a channel cross section is obtained from the solution of the Stokes equation

$$\frac{\partial^2 u}{\partial y^2} = \frac{1}{\mu} \frac{dp}{dx}, \quad (1)$$

where  $p = p(x)$  is the local pressure, subjected to the symmetry condition on the axis of symmetry and the non-slip condition on the upper wall:

$$\left. \frac{\partial u}{\partial y} \right|_{y=0} = 0, \quad u(x, y)|_{y=0.5h(x)} = 0. \quad (2)$$

In Eq. (1)  $\mu$  is the gaseous viscosity. By integrating twice Eq. (1) with the boundary conditions according to Eq. (2) one obtains the streamwise velocity as

$$u(x, y) = -\frac{1}{2\mu} \frac{dp}{dx} \left( \left( \frac{h}{2} \right)^2 - y^2 \right). \quad (3)$$

The mass flow rate is obtained by integrating the velocity profile over the channel cross section

$$\dot{M} = 2w \int_0^{0.5h(x)} \rho u(x, y) dy, \quad (4)$$

whereby  $\rho$  is the density of the gas. Taking account of the state equation of an ideal gas  $\rho = p/(RT)$ , with  $R$  the specific gas constant, the previous equation yields

$$\dot{M} = -\frac{2}{3} w \frac{p}{\mu RT} \frac{dp}{dx} \left( \frac{h}{2} \right)^3. \quad (5)$$

Using the property of the mass conservation in any channel cross section and integrating expression (5) from 0 to  $L$  we obtain

$$\dot{M}^H = \frac{p_1^2 - p_2^2}{12\mu RTL} w \frac{h_1^2 h_2^2}{h_1 + h_2}, \quad (6)$$

giving us an analytical expression for the mass flow rate through the channel in the hydrodynamic regime.

To obtain the previous expression, we assumed here that the local channel height  $h = h(x)$  varies constantly along the channel

$$h(x) = h_1 + \frac{x}{L} (h_2 - h_1). \quad (7)$$

This assumption is made for the further comparison with experimental data. The developed approach, however, can be applied for the case of the other dependencies (non-linear) of the local channel height from the longitudinal coordinate.

Let us consider now the slip flow regime. In this case, the second of the two boundary conditions (2) for the

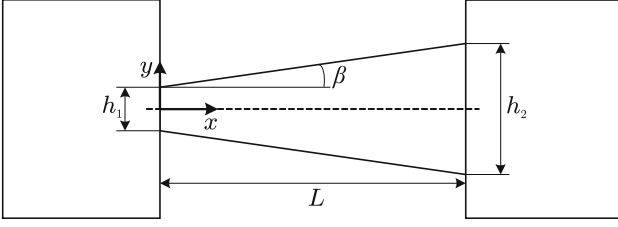


**Fig. 1** Lateral cross section of the tapered channel. The width  $w$  is supposed to remain constant and is large compared to  $h(x)$ . In positive  $x$ -direction, the channel is referred to as a *diffusor*, whereas in negative  $x$ -direction, it is termed *nozzle*

Stokes equation (1) must be changed in slip boundary condition in the form

$$u(x, y) \Big|_{y=0.5h(x)} = -\sigma_p \frac{\mu}{p} \sqrt{2RT} \cos \beta \left( \frac{\partial u}{\partial y} \right) \Big|_{y=0.5h(x)}, \quad (8)$$

$$\beta = \arctan(0.5(h_2 - h_1)/L).$$

This boundary condition takes account of the different inlet and outlet cross-sectional areas by means of the angle  $\beta$  (see Fig. 1). In case of  $h_2 = h_1$  Eq. (8) yields the well-known slip boundary condition for uniform ducts. In the previous equation  $\sigma_p$  is the velocity slip coefficient. In the case of the diffuse reflection of the molecules from the surface, its value was obtained from the solution of the BGK (Albertoni et al. 1963), S-model (Siewert and Sharipov 2002) and the Boltzmann (Ohwada et al. 1989) kinetic equations. So obtained values of the  $\sigma_p$  coefficient lie in the narrow range  $0.968 \leq \sigma_p \leq 1.03$ .

By integrating the Stokes equation with the symmetry boundary condition [first expression in Eq. (2)] and velocity slip boundary condition according to Eq. (8), the streamwise velocity is obtained as

$$u(x, y) = -\frac{1}{2\mu} \frac{dp}{dx} \left( \frac{h}{2} \right)^2 - y^2 + 2\sigma_p \frac{\mu}{p} \sqrt{2RT} \cos \beta \left( \frac{h}{2} \right). \quad (9)$$

The mass flow rate through a cross section is found by replacing in Eq. (4) the velocity expression according to Eq. (9):

$$\dot{M} = -\frac{pw}{\mu RT} \frac{dp}{dx} \left[ \frac{2}{3} \left( \frac{h}{2} \right)^3 + 2\sigma_p \frac{\mu}{p} \sqrt{2RT} \cos \beta \left( \frac{h}{2} \right)^2 \right]. \quad (10)$$

In order to deduce mass flow rate values from the reservoir pressures, it is necessary to integrate Eq. (10) along the channel from 0 to  $L$ , as it was done for Eq. (5). But here the calculation is not so easy as that of Eq. (5). To obtain an explicit expression for the mass flow rate in the slip flow regime, let us first introduce the Knudsen number

$$Kn = \lambda/h_1, \quad \text{where} \quad \lambda = k_\lambda \frac{\mu}{p} \sqrt{2RT}. \quad (11)$$

Here  $\lambda$  is the molecular mean free path,  $k_\lambda$  is the coefficient which depends on the molecular interaction model. Then, the dimensionless variables are defined as following

$$X = \frac{x}{L}, \quad H = \frac{h}{h_1}, \quad P = \frac{p}{p_0}, \quad Q = \dot{M} \frac{\mu(T)RTL}{p_0^2 (0.5h_1)^3 w}, \quad (12)$$

where the average pressure  $p_0 = 0.5(p_1 + p_2)$ . Using these dimensionless variables, the mass flow rate in the hydrodynamic regime, Eq. (6), is transformed into the following non-dimensional form:

$$Q^H = \frac{2}{3} z (P_1^2 - P_2^2) \frac{H_2^2}{H_2 + 1}, \quad (13)$$

where  $H_2 = h_2/h_1$ .

To obtain the mass flow rate in the slip flow regime, Eq. (10) is transformed into a non-dimensional form using relations (12)

$$Q = -\frac{2}{3} H(X)^2 \left( P \frac{dP}{dX} H(X) + bKn \frac{dP}{dX} \right), \quad (14)$$

where the Knudsen number is defined according to Eq. (11). Finally the coefficient  $b$  yields

$$b = 6 \frac{\sigma_p \cos \beta}{k_\lambda}. \quad (15)$$

Then, we eliminate the  $X$  variable, using the  $H(X)$  profile as stated in Eq. (7): i.e.  $dH = (H_2 - 1)dX$ . In the transformed equation, we introduce a double variable change: first using  $Z = 1/H$ , and so transforming Eq. (14) into a classical homogeneous first-order differential equation following  $P(Z)$ . Then to solve this new  $P(Z)$  equation, the classical way is the use of a new function change:  $\Pi(Z) = P/Z$ . Thus, the equation is finally integrated along the  $X$  axis, from 0 to 1.

We omit here the relatively long calculations with rather cumbersome expressions, and we will give only the results. As it was mentioned above, we can distinguish two directions: the *diffusor* and the *nozzle* directions as noted in the caption of Fig. 1.

### 2.3 Diffusor configuration

In the case of the diffusor configuration, after the previously described double variable changes and after integration from 0 to 1, Eq. (14) reads:

$$K \ln(H_2) = \gamma_2 \ln \left( \frac{H_2 - \gamma_1}{H_1 - \gamma_1} \right) - \gamma_1 \ln \left( \frac{H_2 - \gamma_2}{H_1 - \gamma_2} \right), \quad (16)$$

where

$$K^2 = (bKn_0)^2 + 6Q/(H_2 - 1),$$

$$\gamma_1 = -0.5bKn_0 + 0.5K, \quad \gamma_2 = -0.5Kn_0 - 0.5K. \quad (17)$$

Here  $\Pi_1$  and  $\Pi_2$  are the values of function  $\Pi$  calculated for the inlet and outlet cross sections,  $Kn_0$  is the Knudsen number according to Eq. (11), calculated with  $p = p_0$ . Theoretically  $Q$  may be obtain directly from (16) through expression of  $K$  [see Eq. (17)], but  $K$  is implicitly included in different terms of Eq. (16), and therefore, it is difficult to obtain it analytically. Therefore, we linearize Eq. (16) according to the Knudsen number. Indeed, the present analytical method is only pertinent in the slip flow regime and the boundary condition (8) is a first order in Knudsen number condition: thus, in anyway only a first-order Knudsen number precision is implicitly guaranteed on the parameter extracted from Eq. (16). Thus, changing in fact the unknown function we put

$$Q^{\text{dif}} = Q^H(1 + \mathcal{A}^{\text{dif}}Kn_0), \quad (18)$$

then  $K$ , and thus  $\gamma_1$  and  $\gamma_2$  are so linearized and  $\mathcal{A}^{\text{dif}}$  is finally obtained from an algebraic equation of first power following  $\mathcal{A}^{\text{dif}}Kn_0$ .

After long but trivial calculations we obtain:

$$\mathcal{A}^{\text{dif}} = b \left[ \frac{(P_2^2 H_2^2 - B^2)(P_1^2 - B^2)}{2B(P_1 - P_2 H_2)} \ln \frac{(P_1 + B)(P_2 H_2 - B)}{(P_1 - B)(P_2 H_2 + B)} + P_1 P_2 H_2 + B^2 \right] / (P_1 + P_2 H_2) / B^2, \quad (19)$$

where

$$B^2 = \frac{3}{2} \frac{Q^H}{H_2 - 1}. \quad (20)$$

#### 2.4 Nozzle configuration

In the case of the nozzle configuration, the variable changes performed for Eq. (14) lead finally to a complete equation, different from Eq. (16), but of the same complexity: the difference is due to the different sign of  $dH/dX$ . We effectuate then the same linearization process as described above, i.e.:

$$Q^{\text{noz}} = Q^H(1 + \mathcal{A}^{\text{noz}}Kn_0). \quad (21)$$

In a same way as in the diffusor direction case, we obtain

$$\mathcal{A}^{\text{noz}} = b \left[ \frac{((P_1 H_2)^2 + B^2)(P_2^2 + B^2)}{B(P_1 H_2 - P_2)} \left( \arctan \left( \frac{P_1 H_2}{B} \right) - \arctan \left( \frac{P_2}{B} \right) \right) - (P_1 P_2 H_2 + B^2) \right] / (P_1 H_2 + P_2) / B^2. \quad (22)$$

Of course, as expected from our previous comments, the  $\mathcal{A}$  first-order coefficients are different depending on the flow direction.

#### 2.5 Diodicity

In order to define an explicit value for the disparity in both flow directions, we introduce the diodicity  $D$  as the ratio of the mass flow rates  $\dot{M}$  to the difference of the squaring of the inlet and outlet pressures:

$$D = \frac{\dot{M}^{\text{noz}} / \left( (p_1^{\text{noz}})^2 - (p_2^{\text{noz}})^2 \right)}{\dot{M}^{\text{dif}} / \left( (p_1^{\text{dif}})^2 - (p_2^{\text{dif}})^2 \right)}, \quad (23)$$

where  $p_1^{\text{dif}}$ ,  $p_2^{\text{dif}}$ ,  $p_1^{\text{noz}}$ ,  $p_2^{\text{noz}}$  are the inlet and outlet pressure for the diffusor and nozzle directions, respectively. Using expressions (12), (13), (18), (21) and assuming that the inlet and outlet pressures are the same for the diffusor and nozzle cases, the diodicity of a moderately rarefied gas flow becomes

$$D = \frac{1 + \mathcal{A}^{\text{noz}}Kn_0}{1 + \mathcal{A}^{\text{dif}}Kn_0}. \quad (24)$$

Hence, we obtain a predictive expression for  $D$  being a function only of the Knudsen number and the  $\mathcal{A}$  first-order coefficients according to Eqs. (19) and (22). From Eq. (24), it can be seen that  $D$  approaches unity with decreasing rarefaction ( $Kn \rightarrow 0$ : hydrodynamic flow regime). This result is in agreement with that obtained in the hydrodynamic regime: from Eqs. (12) and (13), it is clear that the mass flow rate does not depend on the direction of perfusion.

In Sect. 5, the solutions obtained by means of the analytical approach are compared to a numerical approach addressed in the following section and in detail presented in Graur and Ho (2014). Both approaches are used to calculate the mass flow rate through a tapered channel, and these numerical results are compared with experimental data.

### 3 Numerical approach

The numerical approach (Graur and Ho 2014) is based on the implementation of the solution of the linearized

S-model kinetic equation, obtained in (Sharipov 1999; Graur and Ho 2014). One additional assumption is needed when applying the linearized kinetic equation: the reduced

pressure gradient has to be small in any cross section of the channel

$$\frac{h}{p} \frac{dp}{dx} \ll 1, \quad (25)$$

where  $x$  is the longitudinal coordinate in the flow direction with the origin in the first reservoir, see Fig. 1. It is to note that condition (25) is always satisfied for the microchannels:

$$\frac{h}{p} \frac{dp}{dx} \sim \frac{h}{p} \frac{|p_1 - p_2|}{L} = \frac{h}{L} \frac{|p_1 - p_2|}{p} \ll 1. \quad (26)$$

The last expression in Eq. (26) is always satisfied because for the microchannel  $h \ll L$  and therefore condition (25) is satisfied for any pressure gradient.

Then using the data (Sharipov 1999; Graur and Ho 2014) on the dimensionless coefficient  $G(\delta)$  for various  $h/w$  ratios and the simple interpolation method (Graur and Ho 2014), the mass flow rate is obtained from the differential equation

$$\dot{M} = - \frac{h^2 w}{\sqrt{2RT}} G_p(\delta, h/w) \frac{dp}{dx}, \quad (27)$$

that is solved by means of the shooting method. In Eq. (27) the dimensionless coefficient  $G_p$  depends on the channel height to width ratio  $h/w$ , local channel height  $h$  and the gas rarefaction parameter (local pressure), which is calculated according to

$$\delta = \frac{hp}{\mu\sqrt{2RT}}. \quad (28)$$

It is to note that this rarefaction parameter is inversely proportional to the Knudsen number  $\delta \sim 1/Kn$ , see Eq. (11). The detailed description of this approach may be found in Graur and Ho (2014). It is to underline that contrarily to the analytical approach, presented in Sect. 2.2, this numerical method allows to obtain the mass flow rate for any values of the Knudsen numbers laying from the hydrodynamic to the free molecular flow regime.

In order to compare both approaches, the resulting mass flow rates of carbon dioxide, nitrogen and argon for several values of the inlet and outlet pressures are given in Tables 2, 3, 4, 5, 6 and 7 (in ‘‘Appendix’’) for the diffusor and nozzle flows, respectively. Also, the deviation of the numerical simulation from the experiment is provided in Tables 2, 3, 4, 5, 6 and 7, too. The experiment is described in the following section.

## 4 Experiment

### 4.1 Microchannel manufacturing

The tapered channel with alongside varying height was manufactured by milling a long notch into a piece of

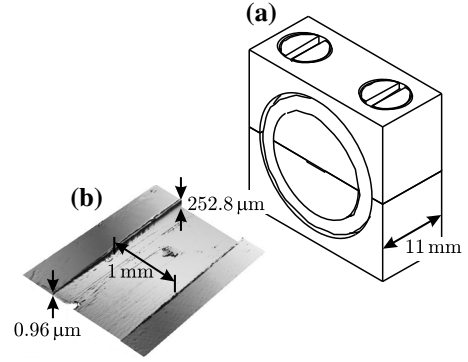


**Fig. 2** Tapered channel used in this work. The test channel accrues by assembling one aluminum block with a micromilled notch with a plain block (a). The channel length corresponds to the block thickness. High-quality optical surfaces act as sealing. The channel with alongside varying height is visualized by optical profilometry (b)

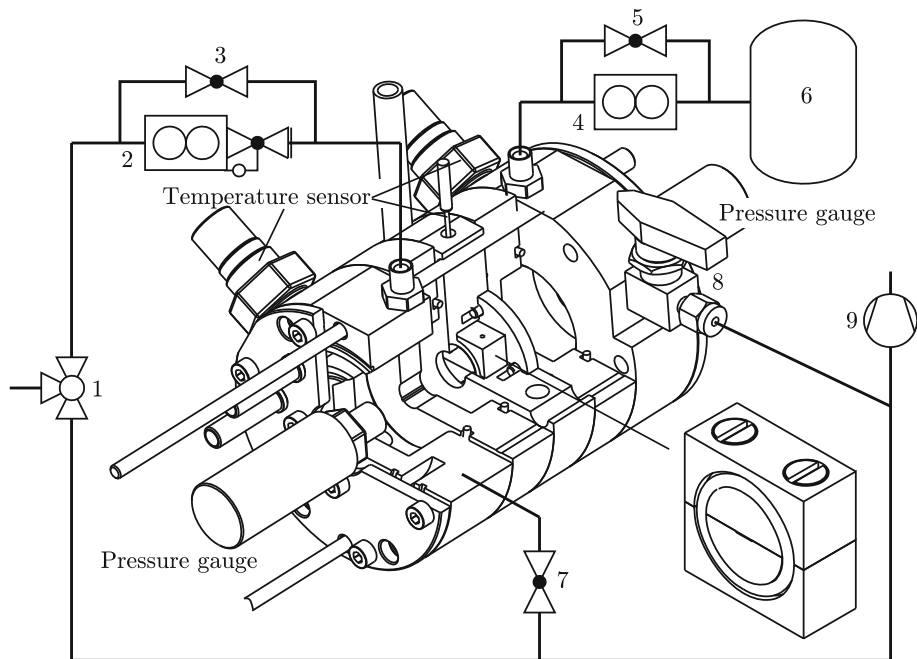
aluminum ( $AlMg_3$ ) using raster fly-cutting. As schematically shown in Fig. 2a, the notch was capped with another plain piece of aluminum with high-quality optical surface. Both parts were screwed together and sealed by means of the perfectly plain surfaces. All parts were manufactured by the LFM (Laboratory for Precision Machining, University of Bremen) using a Nanotech 350FG (Moore Nanotechnology Systems, Keene, NH, USA). The micromilled notch with a significant inclination was visualized by optical profilometry Fig. 2b.

The notch of the channel has a length of  $L = 11.05 \pm 0.1$  mm which corresponds to the thickness of the aluminum block. The height is changing from  $h_1 = 0.96 \pm 0.18$  to  $h_2 = 252.80 \pm 0.16$   $\mu\text{m}$  while the width of  $w = 1,007.50 \pm 3.13$   $\mu\text{m}$  is constant, see also Fig. 1. Notch width and depth were measured 200 times using optical profilometry (PL  $\mu$ 2300, Sensofar), and arithmetic mean and uncertainty were calculated. The length was measured by means of direct light microscopy (20 times for calculation of arithmetic mean and uncertainty).

### 4.2 Mass flow rate measurement

Figure 3 gives a sectional drawing of the experimental apparatus embedded in the process flow diagram of the setup. The apparatus consists of two chambers in which temperature was measured by PT1000 resistance thermometers (WIKA, TF35) and absolute pressure was measured by a pressure gauge (GE Sensing, PMP4070). The inlet of the upstream chamber was connected to the gas supply (1) via a mass flow controller (2) (Bronckhorst, F-201CV-ABD-11-Z). The outlet of the downstream chamber was connected to a vessel (6) with a volume of 15 l by a mass flow sensor (4) (Bronckhorst, F-110C-002-AGD-11-V). Both the mass flow sensor (MFS) and mass

**Fig. 3** Sectional drawing of the experimental apparatus embedded in the process flow diagram of the setup. Beyond the termed elements, the setup includes: gas supply valve (1); mass flow controller (2); bypass valve (3, 5); mass flow sensor (4); pressure vessel (6); ball valve (7, 8); vacuum pump (9). The test channel according to Fig. 2 used for the experiments can be assembled in both directions (convergent/divergent) into the apparatus



flow controller (MFC) can be bypassed (valves 3 and 5) for evacuating and cleaning of the overall system. Furthermore, both chambers have a second connection to a vacuum pump (9) via ball valves 7 and 8 for this very purpose. A more extensive description of the experimental apparatus is given in Veltzke (2013).

The test procedure was as follows. The apparatus shown in Fig. 3 was brought to the constant operation temperature. Valves 3, 5, 7 and 8 were opened and the complete system was evacuated by the vacuum pump (9) to a pressure of 0.1 kPa while the gas supply was closed. Then, the system was filled with the current working gas ( $\text{CO}_2$ ,  $\text{N}_2$ , Ar) to a pressure of 150 kPa. Afterward, the supply valve was closed and the vacuum pump was switched on again. This procedure was repeated 10 times to ensure that the contamination of the system with other gases was negligible. After this preparatory cleaning procedure, the system was brought to the desired working pressure and valves 3, 5, 7 and 8 were closed.

The mass flow rate measurements were performed by controlling the pressure difference via the MFC. When the mass flow rate reached steady state, data (mass flow rate, inlet pressure and temperature, outlet pressure and temperature) was logged and averaged over 10 min. Afterward, the next pressure difference was adjusted. Each single series of measurements was performed in triplicate for stochastic validation. All results are given in Tables 2 and 7 in the “Appendix”.

## 5 Results and discussion

The analytical and numerical simulations are carried out for the tapered channel according to Fig. 1. This configuration is slightly different from that used for the measurements which is due to the manufacturing process as described in Sect. 4.1. From the measurement, both inlet and outlet temperatures are identical, and therefore, the flow can be considered as the isothermal flow and the average temperature value  $T_0 = 0.5(T_1 + T_2)$  was taken for the simulations. For a calculation of  $\dot{M}$  the velocity slip coefficient  $\sigma_p$  in Eq. (8) was set to 1.016 for all three gases. It is to note that this value  $\sigma_p \sim 1$  corresponds to the completely diffuse reflection of the molecules from the solid surface. This value increases when the reflection becomes more specular. Some experimental data on the values of the velocity slip for different surfaces and various gases may be found (Graur et al. 2009; Perrier et al. 2011).

### 5.1 Validation of analytical approach

First, expressions (18)–(22) are used to obtain the analytical solutions in diffusor and nozzle directions. The Variable Hard Sphere model (VHS) (Bird 1994) is used as the intermolecular potential which leads to the following expression of the  $k_\lambda$  coefficient in Eq. (11):  $k_\lambda = (7 - 2\omega)(5 - 2\omega)/(15\sqrt{\pi})$ . For the viscosity, the power law dependence from temperature according to the VHS is adopted

**Table 1** Properties of gases used for experiments

Gas	$R$ (J kg <sup>-1</sup> K <sup>-1</sup> )	$\mu_{\text{ref}}$ (10 <sup>-5</sup> Pa s)	$\omega$	$k_i$
CO <sub>2</sub>	188.96	1.380	0.93	0.607
N <sub>2</sub>	296.93	1.656	0.74	0.731
Ar	207.85	2.117	0.81	0.684

The reference viscosities are those for  $T_{\text{ref}} = 273.15$  K  
Values are taken from Bird (1994)

$$\mu = \mu_{\text{ref}} \left( \frac{T}{T_{\text{ref}}} \right)^{\omega} \quad (29)$$

Here  $\omega$  is the viscosity index depending on the gas nature. The required parameters  $\omega$  and  $\mu_{\text{ref}}$  for  $T_{\text{ref}} = 273.15$  K are stated in Table 1.

As shown in Fig. 4, the analytical, numerical, and experimental results are in good agreement for the diffusor case. In the nozzle direction, however, the both numerical and analytical approaches systematically overestimate the experimental results, see Tables 2, 3, 4, 5, 6 and 7. For all gases, it can be observed that the mass flow rate in nozzle direction is slightly but significantly higher compared to the diffusor direction. This is a reasonable result since the amount of molecules entering the channel aperture (cross-sectional area) is higher. Nevertheless, the finding is indeed intriguing because it vanishes in the hydrodynamic regime (Veltzke 2013; Veltzke et al. 2012) and is postulated to be absent in the free molecular regime (Sharipov and Bertoldo 2005; Graur and Ho 2014).

Further, the reasonable agreement of the analytical model to the numerical model and the experiments (see

Tables 2, 3, 4, 5, 6, 7 in “Appendix” and Fig. 4) indicates the validity of the presented approach. It is noteworthy that the analytical solutions are obtained here in the Knudsen number range from 0.0471 to 0.2263, where the highest value is really in the limit of the applicability of the approach. However, even for this relatively high Knudsen number, the agreement with the measurements is surprisingly good.

## 5.2 Gas flow diodicity

As shown by means of Fig. 4, the measured flow in nozzle direction is throughout higher compared to the flow in diffusor direction. To quantify the disparity of the permeability in both directions, we use the diodicity  $D$  given by Eq. (23). For the calculation of the experimental diodicity, the mean values of three identical measurement series were used. Since Eq. (23) contains six measured values, the standard deviation of  $D$  is calculated according to the Gaussian error propagation:

$$\xi(D) = \sqrt{\sum_{i=1}^6 \left( \frac{\partial D}{\partial z_i} \xi(z_i) \right)^2}; \quad z = p_1^{\text{noz}}, p_2^{\text{noz}}, p_1^{\text{dif}}, p_2^{\text{dif}}, \dot{M}^{\text{noz}}, \dot{M}^{\text{dif}}. \quad (30)$$

We want to show and discuss the diode effect as a function of the gaseous rarefaction. Therefore, we use the Knudsen number according to Eq. (11) as abscissa value. To allow for comparison of nozzle and diffusor direction, we define  $\bar{Kn}$  by means of the average pressure values of nozzle and diffusor directions  $\bar{p} = 0.25(p_1^{\text{noz}} + p_2^{\text{noz}} + p_1^{\text{dif}} + p_2^{\text{dif}})$ . Thus,  $\bar{Kn}$  is a

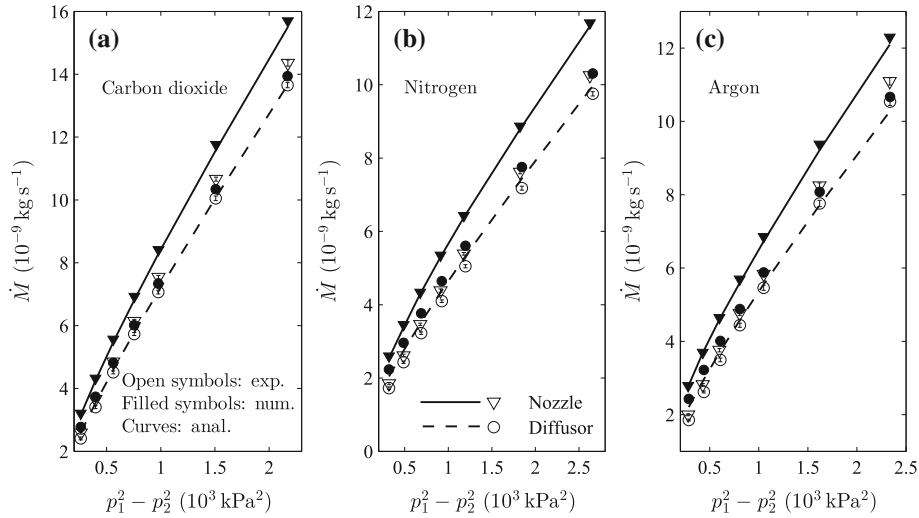


**Fig. 4** Experimental data in comparison with the proposed analytical approach and data obtained numerically using method of Graur and Ho (2014): **a** carbon dioxide; **b** nitrogen; **c** argon. The curves for the analytical solutions in nozzle direction (solid line) and diffusor

direction (dashed line) are obtained using expressions (18)–(22). Measurements were performed in triplicate under isothermal conditions at 20 °C. Error bars are throughout smaller than symbols. Data are additionally provided in Tables 2, 3, 4, 5, 6 and 7 in the “Appendix”

function of five measured values having errors and its uncertainty is obtained as

$$\xi(\bar{Kn}) = \sqrt{\sum_{i=1}^5 \left( \frac{\partial \bar{Kn}}{\partial z_i} \xi(z_i) \right)^2}; \quad z = p_1^{\text{noz}}, p_2^{\text{noz}}, p_1^{\text{dif}}, p_2^{\text{dif}}, h_1. \quad (31)$$

All values obtained for  $D$  (as a function of  $\bar{Kn}$ ) by means of the numerical approach and experiments are provided in Tables 8, 9 and 10 in the ‘‘Appendix’’.

In Fig. 5, the diodicity  $D$  is plotted versus the average Knudsen number  $\bar{Kn}$  for all three working gases. The analytical solutions obtained by means of Eq. (24) are given by solid lines, and the numerical results obtained applying model of Graur and Ho (2014) are indicated by filled symbols. The experimental results indicated by open symbols and error bars are calculated using Eqs. (11) and (23). For the three considered gases, the analytical and the numerical approach are in qualitative agreement to the experiment since both theoretical approaches show that the diode effect increases with gaseous rarefaction in slip regime.

When comparing first the numerical approach with the experiments, we can see that  $D$  approaches a constant level at approx.  $\bar{Kn} = 0.15$ . It is to note that the numerical approach reproduces the experimental behavior very well: the numerical results exhibit an offset of approx. 8 % (see Tables 8, 9, 10) that is quite constant. The offset is

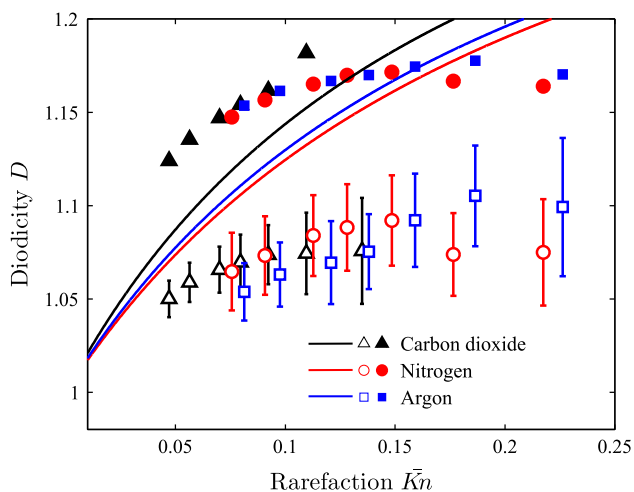


**Fig. 5** Diodicity versus mean Knudsen number. Analytical data (solid lines) is calculated according to Eqs. (19), (22), (24). Numerical data (filled symbols) and experimental data (open symbols) are prepared according to Eqs. (11) and (23) with values stated in Tables 2, 3, 4, 5, 6 and 7 in ‘‘Appendix’’. The experimental uncertainty is expressed by error bars that are calculated according to Eqs. (30) and (31) whereby horizontal error bars are throughout smaller than symbols. In addition, all depicted values are provided in Tables 8, 9 and 10 in the ‘‘Appendix’’

explained by the larger systematic overestimation of the nozzle experimental data discussed in the context of Fig. 4.

In contrast, the analytical approach cannot describe the attenuation of  $D$ . In the full slip regime, the analytical solution is in reasonable agreement to the experimental results that are slightly overestimated. Although, with increasing  $\bar{Kn}$  the overestimation would become very large. This might be due to the limited validity of the analytical approach. As already mentioned in Sect. 5.1, the applicability of the approach concerning rarefaction is at its very limit.

Nevertheless, the theoretical and experimental finding perfectly confirms our considerations stated in Sect. 1 and verifies the reliability of both approaches for the considered Knudsen number range. From the analysis presented here, we are sure that the gas flow diode effect is not an artifact because it is found analytically, numerically and experimentally. Furthermore, the finding is in agreement with results obtained on tapered silicon-etched microchannels (Veltzke 2013; Veltzke et al. 2012).

A complete physical explanation of the diode effect is probably complex. But some comments may be proposed. The diode feature does not exist in the hydrodynamic regime and vanish in the free molecular regime. Thus, this effect appears when a gas slip velocity and a sufficient gas density allow a transfer, more or less important, of macroscopic momentum from the wall to the gas flow. However, it would be more difficult to explain clearly why the nozzle configuration promotes larger mass flow rate than the diffusor one. The complete understanding of the gas flow diode effect remains an interesting topic for future work.

## 6 Conclusion

In this work, we apply three approaches, an experimental, an analytical and a numerical one, that allow us to confirm and describe the phenomenon of gas flow diodicity. By means of the two theoretical approaches, we could predict the mass flow rate through a long channel with variable rectangular cross section for arbitrary pressure gradients. Solutions obtained by means of both models are compared with one another and with experimental data for validation purpose.

The analytical approach based on the solution of the Stokes equation subjected to the velocity slip boundary condition is developed for the slip flow regime. The numerical approach is based on the implementation of the solution of the linearized S-model kinetic equation obtained previously in (Sharipov 1999; Graur and Ho 2014). For the experiments, we used single-gas measurements obtained on a rectangular channel with slightly varying cross section.

The test channel was manufactured by micromilling (raster fly-cutting). It is noteworthy that this is a novel method for production of test channels for research on gaseous microflows.

All the numerical and analytical results are in good agreement to the experimental ones although experimental data are systematically overestimated in the nozzle case.

Moreover, we can show that the mass flow rate is significantly higher when the tapered channel is perfused like a nozzle. It can therefore be stated that under moderately rarefied conditions, microsized ducts with alongside varying cross section act as a gas flow diode. The theoretically and experimentally analyzed diode effect increases with gaseous rarefaction whereby both presented models can predict that effect qualitatively.

The analyzed diode effect is primarily a physical phenomenon and hence an academic issue. However, it might be applicable in future MEMS if the diodicity can be pushed to pronounced values. Probable applications are devices for dosing and pumping gas streams or actual diodes that only allow the flow in one direction.

**Acknowledgments** Some of the presented results are based on a project funded by German Federal Ministry of Economics and Technology (BMW) according to a decision of the German Federal Parliament; funding code 0327512A. One of the authors (Thomas Veltzke) wants to thank Georg Grathwohl for his support.

## Appendix

See Tables 2, 3, 4, 5, 6, 7, 8, 9 and 10.

**Table 2** Experimental results obtained in *diffuser* direction on the tapered channel according to Fig. 2 with CO<sub>2</sub> as working gas, analytical solution, numerical solution

$p_1$ (kPa)	$p_2$ (kPa)	$T_0$ (°C)	$\dot{M}$ ( $10^{-9}$ kg s $^{-1}$ )			$\alpha$ (%)
			Exp.	Anal.	Num.	Num.
23.0389 ± 0.0963	3.0266 ± 0.1010	20.7832	2.411 ± 0.047	2.5967	2.7737	11.1
28.3679 ± 0.0852	3.3626 ± 0.0966	20.7963	3.404 ± 0.045	3.5363	3.7358	7.6
33.7133 ± 0.0746	3.7084 ± 0.0904	20.8247	4.513 ± 0.047	4.5994	4.8180	5.4
39.0586 ± 0.0887	4.0720 ± 0.0924	20.8529	5.733 ± 0.049	5.7832	6.0150	3.8
44.4236 ± 0.0821	4.4461 ± 0.0912	20.8748	7.067 ± 0.059	7.0935	7.3368	2.8
55.1305 ± 0.0816	5.1696 ± 0.0879	20.9017	10.049 ± 0.074	10.0770	10.3402	2.2
66.1574 ± 0.0712	5.9404 ± 0.0826	20.9150	13.653 ± 0.080	13.6606	13.9404	1.6

Measurements were performed in triplicate and arithmetic mean and standard deviation are calculated. The deviation  $\alpha$  of the numerical solution to the experimental results is:  $|(\dot{M}_{\text{exp}}/\dot{M}_{\text{num}}) - 1| \cdot 100 \%$

**Table 3** Experimental results obtained in *nozzle* direction on the tapered channel according to Fig. 2 with CO<sub>2</sub> as working gas, analytical solution, numerical solution

$p_1$ (kPa)	$p_2$ (kPa)	$T_0$ (°C)	$\dot{M}$ ( $10^{-9}$ kg s $^{-1}$ )			$\alpha$ (%)
			Exp.	Anal.	Num.	Num.
23.0154 ± 0.0460	3.0140 ± 0.0355	20.9951	2.588 ± 0.042	3.1490	3.2094	17.9
28.3678 ± 0.0530	3.3753 ± 0.0385	20.9844	3.656 ± 0.052	4.2488	4.3256	14.1
33.7229 ± 0.0596	3.7466 ± 0.0404	20.9753	4.847 ± 0.046	5.4706	5.5643	11.9
39.0837 ± 0.0633	4.1230 ± 0.0461	20.9804	6.139 ± 0.061	6.8157	6.9264	10.4
44.4619 ± 0.0603	4.5079 ± 0.0467	20.9771	7.542 ± 0.053	8.2878	8.4152	9.7
55.1912 ± 0.0522	5.2426 ± 0.0383	20.9761	10.662 ± 0.065	11.5988	11.7585	8.8
66.2069 ± 0.0694	6.0228 ± 0.0429	20.9728	14.354 ± 0.099	15.5064	15.6962	8.3

Measurements were performed in triplicate and arithmetic mean and standard deviation are calculated. The deviation  $\alpha$  of the numerical solution to the experimental results is:  $|(\dot{M}_{\text{exp}}/\dot{M}_{\text{num}}) - 1| \cdot 100 \%$

**Table 4** Experimental results obtained in *diffusor* direction on the tapered channel according to Fig. 2 with N<sub>2</sub> as working gas and the analytical solution

$p_1$ (kPa)	$p_2$ (kPa)	$T_0$ (°C)	$\dot{M}$ ( $10^{-9}$ kg s $^{-1}$ )			$\alpha$ (%)
			Exp.	Anal.	Num.	Num.
25.5150 ± 0.0867	3.3040 ± 0.1093	20.0523	1.722 ± 0.033	2.0485	2.2331	22.8
31.4279 ± 0.0709	3.6811 ± 0.1040	20.1392	2.431 ± 0.032	2.7506	2.9589	17.8
37.3339 ± 0.0403	4.0762 ± 0.0948	20.0546	3.223 ± 0.033	3.5313	3.7636	14.4
43.2610 ± 0.0577	4.4717 ± 0.0983	20.1423	4.095 ± 0.035	4.3956	4.6440	11.8
49.1804 ± 0.0299	4.8795 ± 0.0947	20.0642	5.048 ± 0.042	5.3390	5.6054	9.9
61.0077 ± 0.0688	5.6739 ± 0.0949	20.0645	7.178 ± 0.052	7.4670	7.7559	7.5
73.2224 ± 0.0504	6.5315 ± 0.0883	20.1556	9.751 ± 0.057	10.0020	10.3086	5.4

Measurements were performed in triplicate and arithmetic mean and standard deviation are calculated. The deviation  $\alpha$  of the numerical solution to the experimental results is:  $|(\dot{M}_{\text{exp}}/\dot{M}_{\text{num}}) - 1| \cdot 100 \%$

**Table 5** Experimental results obtained in *nozzle* direction on the tapered channel according to Fig. 2 with N<sub>2</sub> as working gas and the analytical solution

$p_1$ (kPa)	$p_2$ (kPa)	$T_0$ (°C)	$\dot{M}$ ( $10^{-9}$ kg s $^{-1}$ )			$\alpha$ (%)
			Exp.	Anal.	Num.	Num.
25.4982 ± 0.0971	3.3167 ± 0.0455	20.2315	1.848 ± 0.029	2.5404	2.5955	28.8
31.4365 ± 0.0125	3.7172 ± 0.0512	20.2275	2.611 ± 0.037	3.3847	3.4532	24.4
37.0293 ± 0.0503	4.0850 ± 0.0628	20.3197	3.462 ± 0.032	4.2543	4.3363	20.2
42.9162 ± 0.0643	4.4908 ± 0.0728	20.2300	4.384 ± 0.043	5.2483	5.3452	17.9
48.8057 ± 0.0728	4.9114 ± 0.0788	20.3196	5.387 ± 0.037	6.3179	6.4300	16.2
60.6650 ± 0.0935	5.7264 ± 0.0902	20.2143	7.615 ± 0.046	8.7249	8.8676	14.1
72.7721 ± 0.1444	6.5730 ± 0.1134	20.3082	10.252 ± 0.070	11.5088	11.6816	12.2

Measurements were performed in triplicate and arithmetic mean and standard deviation are calculated. The deviation  $\alpha$  of the numerical solution to the experimental results is:  $|(\dot{M}_{\text{exp}}/\dot{M}_{\text{num}}) - 1| \cdot 100 \%$

**Table 6** Experimental results obtained in *diffusor* direction on the tapered channel according to Fig. 2 with argon as working gas and the analytical solution

$p_1$ (kPa)	$p_2$ (kPa)	$T_0$ (°C)	$\dot{M}$ ( $10^{-9}$ kg s $^{-1}$ )			$\alpha$ (%)
			Exp.	Anal.	Num.	Num.
24.1557 ± 1.1984	3.1894 ± 0.0875	20.2224	1.855 ± 0.024	2.2116	2.4310	23.7
29.8508 ± 0.4329	3.5046 ± 0.0691	20.3247	2.619 ± 0.025	2.9672	3.2205	18.7
35.0942 ± 0.3716	3.8842 ± 0.1058	20.2002	3.494 ± 0.050	3.7342	4.0113	12.9
40.4200 ± 0.1979	4.2844 ± 0.0670	20.3037	4.440 ± 0.056	4.5813	4.8815	9.0
46.0627 ± 0.4633	4.6966 ± 0.1051	20.2596	5.459 ± 0.068	5.5608	5.8797	7.1
57.1809 ± 0.3115	5.4635 ± 0.0897	20.3554	7.762 ± 0.085	7.7265	8.0779	3.9
68.6523 ± 0.2623	6.2922 ± 0.0991	20.3771	10.537 ± 0.101	10.2917	10.6655	1.2

Measurements were performed in triplicate and arithmetic mean and standard deviation are calculated. The deviation  $\alpha$  of the numerical solution to the experimental results is:  $|(\dot{M}_{\text{exp}}/\dot{M}_{\text{num}}) - 1| \cdot 100 \%$

**Table 7** Experimental results obtained in *nozzle* direction on the tapered channel according to Fig. 2 with argon as working gas and the analytical solution

$p_1$ (kPa)	$p_2$ (kPa)	$T_0$ (°C)	$\dot{M}$ ( $10^{-9}$ kg s $^{-1}$ )			$\alpha$ (%)
			Exp.	Anal.	Num.	Num.
23.9157 ± 0.2195	3.2167 ± 0.1450	20.4180	1.998 ± 0.025	2.7240	2.7868	28.3
29.4861 ± 0.2912	3.5476 ± 0.1039	20.2266	2.822 ± 0.027	3.6208	3.6981	23.7
34.8385 ± 0.1110	3.9118 ± 0.0803	20.3091	3.759 ± 0.045	4.5492	4.6413	19.0
40.3653 ± 0.1512	4.2902 ± 0.0818	20.2371	4.762 ± 0.054	5.5870	5.6952	16.4
46.0374 ± 0.1320	4.6987 ± 0.0954	20.3179	5.832 ± 0.065	6.7279	6.8531	14.9
57.1578 ± 0.1790	5.4656 ± 0.0827	20.2057	8.245 ± 0.076	9.2151	9.3749	12.0
68.6183 ± 0.2053	6.2951 ± 0.0825	20.3059	11.092 ± 0.103	12.0971	12.2915	9.8

Measurements were performed in triplicate and arithmetic mean and standard deviation are calculated. The deviation  $\alpha$  of the numerical solution to the experimental results is:  $|(\dot{M}_{\text{exp}}/\dot{M}_{\text{num}}) - 1| \cdot 100$  %

**Table 8** Knudsen number and experimental and numerically calculated diodicity of carbon dioxide

$\bar{K}_n$	$D$		$\alpha$ (%)
	Exp.	Num.	Num.
0.1349 ± 8.5e-4	1.0757 ± 0.0139	1.2929	16.8
0.1096 ± 7.1e-4	1.0744 ± 0.0102	1.1818	9.1
0.0922 ± 6.1e-4	1.0737 ± 0.0069	1.1617	7.6
0.0796 ± 5.6e-4	1.0696 ± 0.0064	1.1542	7.3
0.0700 ± 5.0e-4	1.0657 ± 0.0051	1.1470	7.1
0.0564 ± 4.1e-4	1.0589 ± 0.0042	1.1354	6.7
0.0470 ± 3.6e-4	1.0500 ± 0.0039	1.1241	6.6

$\bar{K}_n$  and  $D$  are calculated according to Eqs. (11), (23), (30) and (31) using values stated in Tables 1, 2 and 3

The deviation  $\alpha$  of the numerical solution to the experimental results is:  $|(\bar{D}_{\text{exp}}/\bar{D}_{\text{num}}) - 1| \cdot 100$  %

**Table 9** Knudsen number and experimental and numerically calculated diodicity of nitrogen

$\bar{K}_n$	$D$		$\alpha$ (%)
	Exp.	Num.	Num.
0.2174 ± 9.1e-4	1.0750 ± 0.0140	1.1640	7.6
0.1765 ± 7.7e-4	1.0738 ± 0.0103	1.1667	7.9
0.1485 ± 9.1e-4	1.0921 ± 0.0115	1.1715	6.8
0.1282 ± 8.4e-4	1.0883 ± 0.0109	1.1699	6.9
0.1127 ± 7.7e-4	1.0840 ± 0.0101	1.1651	6.9
0.0907 ± 7.1e-4	1.0732 ± 0.0097	1.1566	7.2
0.0756 ± 6.4e-4	1.0646 ± 0.0096	1.1475	7.2

$\bar{K}_n$  and  $D$  are calculated according to Eqs. (11), (23), (30) and (31) using values stated in Tables 1, 4 and 5

The deviation  $\alpha$  of the numerical solution to the experimental results is:  $|(\bar{D}_{\text{exp}}/\bar{D}_{\text{num}}) - 1| \cdot 100$  %

**Table 10** Knudsen number and experimental and numerically calculated diodicity of argon

$\bar{K}_n$	$D$		$\alpha$ (%)
	Exp.	Num.	Num.
0.2263 ± 2.1e-3	1.0992 ± 0.0390	1.1703	6.1
0.1865 ± 1.3e-3	1.1052 ± 0.0131	1.1777	6.1
0.1590 ± 1.0e-3	1.0922 ± 0.0119	1.1745	7.0
0.1380 ± 8.0e-4	1.0754 ± 0.0092	1.1699	8.1
0.1208 ± 8.6e-4	1.0694 ± 0.0104	1.1669	8.3
0.0975 ± 6.6e-4	1.0631 ± 0.0076	1.1615	8.5
0.0813 ± 5.6e-4	1.0538 ± 0.0067	1.1536	8.6

$\bar{K}_n$  and  $D$  are calculated according to Eqs. (11), (23), (30) and (31) using values stated in Tables 1, 6 and 7

The deviation  $\alpha$  of the numerical solution to the experimental results is:  $|(\bar{D}_{\text{exp}}/\bar{D}_{\text{num}}) - 1| \cdot 100$  %

## References

- Albertoni S, Cercignani C, Gotusso L (1963) Numerical evaluation of the slip coefficient. *Phys Fluids* 6:993
- Aubert C, Colin S (2001) High-order boundary conditions for gaseous flows in rectangular microducts. *Microscale Therm Eng* 5:41–54
- Aubert C, Colin S, Caen R (1998) Unsteady gaseous flows in tapered microchannels. In: *Technical proceedings of the 1998 international conference on modeling and simulation of microsystems*, volume chapter 11: applications: microfluidics, pp 486–491
- Bird GA (1994) *Molecular gas dynamics and the direct simulation of gas flows*. Oxford Science Publications, Oxford University Press Inc., New York
- Colin S, Lalonde P, Caen R (2004) Validation of a second-order slip flow model in a rectangular microchannel. *Heat Transf Eng* 25:23–30
- de Silva LR, Deschamps CJ (2012) Modeling of gas leakage through compressor valves. In: *International compressor engineering conference*, paper 2105

- Ewart T, Perrier P, Graur IA, Méolans JG (2007) Mass flow rate measurements in microchannel, from hydrodynamic to near free molecular regimes. *J Fluid Mech* 584:337–356
- Graur IA, Perrier P, Ghozlani W, Méolans JG (2009) Measurements of tangential momentum accommodation coefficient for various gases in plane microchannel. *Phys Fluids* 21:102004
- Graur I, Ho MT (2014) Rarefied gas flow through a long rectangular channel of variable cross section. *Vacuum* 101:328–332
- Lee HW, Azid HA (2009) Neuro-genetic optimization of the diffuser elements for applications in a valveless diaphragm micropumps system. *Sensors* 9:7481–7497
- Ohwada T, Sone Y, Aoki K (1989) Numerical analysis of the shear and thermal creep flows of a rarefied gas over a plane wall on the basis of the linearized Boltzmann equation for hard-sphere molecules. *Phys Fluids A* 1:1588–1599
- Perrier P, Graur IA, Ewart T, Méolans JG (2011) Mass flow rate measurements in microtubes: from hydrodynamic to near free molecular regime. *Phys Fluids* 23:042004
- Porodnov BT, Suetin PE, Borisov SF, Akinshin VD (1974) Experimental investigation of rarefied gas flow in different channels. *J Fluid Mech* 64:417–437
- Sharipov F, Seleznev V (1998) Data on internal rarefied gas flows. *J Phys Chem Ref Data* 27:657–706
- Sharipov F (1999) Non-isothermal gas flow through rectangular microchannels. *J Micromech Microeng* 9:394–401
- Sharipov F, Bertoldo G (2005) Rarefied gas flow through a long tube of variable radius. *J Vac Sci Technol A* 23:531–533
- Siewert CE, Sharipov F (2002) Model equations in rarefied gas dynamics: viscous-slip and thermal-slip coefficients. *Phys Fluids* 14:4123–4129
- Stemme E, Stemme G (1993) Valve-less diffuser/nozzle based fluid pump. *Sens Actuators A Phys* 39:159–167
- Stevanovic ND (2007) A new analytical solution of microchannel gas flow. *J Micromech Microeng* 17:1695–1702
- Stevanovic ND, Djordjevic VD (2012) The exact analytical solution for the gas lubricated bearing in the slip and continuum flow regime. *Publications de l'Institut Mathématique* 91:83–93
- Titarev VA, Utyuzhnikov SV, Shakhov EM (2013) Rarefied gas flow into vacuum through square pipe with variable cross section. *Comput Math Math Phys* 53:1221–1230
- Veltzke T (2013) On gaseous microflows under isothermal conditions. PhD thesis, University of Bremen
- Veltzke T, Baune M, Thöming J (2012) The contribution of diffusion to gas microflow: an experimental study. *Phys Fluids* 24:082004